Warm dense crystallography

Ryan A. Valenza and Gerald T. Seidler*
Physics Department, University of Washington, 3910 15th Ave. NE, Seattle, Washington 98195-1560, USA
(Received 17 December 2015; published 21 March 2016)

The intense femtosecond-scale pulses from x-ray free electron lasers (XFELs) are able to create and interrogate interesting states of matter characterized by long-lived nonequilibrium semicore or core electron occupancies or by the heating of dense phases via the relaxation cascade initiated by the photoelectric effect. We address here the latter case of "warm dense matter" (WDM) and investigate the observable consequences of x-ray heating of the electronic degrees of freedom in crystalline systems. We report temperature-dependent density functional theory calculations for the x-ray diffraction from crystalline LiF, graphite, diamond, and Be. We find testable, strong signatures of condensed-phase effects that emphasize the importance of wide-angle scattering to study nonequilibrium states. These results also suggest that the reorganization of the valence electron density at eV-scale temperatures presents a confounding factor to achieving atomic resolution in macromolecular serial femtosecond crystallography (SFX) studies at XFELs, as performed under the "diffract before destroy" paradigm.

DOI: 10.1103/PhysRevB.93.115135

I. INTRODUCTION

The development of x-ray free electron lasers (XFELs) is having a broad impact across physics, chemistry, biology, materials science, and other fields [1–4]. Among the unique characteristics of the XFEL pulses are their exceptionally high peak brilliance and short duration properties that allow easy study of x-ray nonlinear effects. While the earliest results in this new branch of x-ray science addressed atomic and small cluster physics [5,6], more recent work has begun to focus instead on the properties of condensed phases upon extreme x-ray exposure [7–11].

In x-ray heating experiments using femtosecond-scale pulse durations, characterization of the resulting state is predominantly based on x-ray diagnostics, either as a consequence of interaction with the initial heating pulse itself [5–7,9] or by a second pulse in purely x-ray pump-probe "two color" experiments that have recently become possible [12–14]. The primary experimental observables of x-ray diagnostics are the momentum-space electronic distribution, as embodied in Compton scattering [15,16], the occupancies of various core and valence quasiparticle states, as probed by x-ray spectroscopies [17], and finally the real-space charge distribution $\rho(\vec{r})$, which is directly interrogated by x-ray diffraction (XRD) [18,19].

We focus here on $\rho(\vec{r})$ and the consequent XRD for several reasons. First, $\rho(\vec{r})$ and its temperature dependence plays an important qualitative role in constraining the assumptions underlying theoretical treatments of ionization potential (IP) suppression: if the high-T (many eV) valence electron contribution to $\rho(\vec{r})$ is strongly inhomogeneous due to condensed phase effects, then one must move well beyond the mean-field, jelliumlike screening approaches that have been inherited from low-density plasma physics [20–23]. The influence of charge inhomogeneity on IP suppression has been previously investigated via Density Functional Theory (DFT) calculations by Vinko *et al.* [24], and has been demonstrated in experiments at the Linac Coherent Light Source (LCLS) by Ciricosta *et al.* [25]. In the aforementioned studies, the primary diagnostic of interest was x-ray emission spectroscopy, whereas, in this paper, we are concerned with the effects of charge inhomogeneity within crystalline systems, where XRD gives the most direct characterization of the primary quantum mechanical observable, $\rho(\vec{r})$. Second, while our predictions of inhomogeneous charge rearrangement in crystalline warm dense matter run contrary to much prior work in the field, similar effects have been seen in the condensed matter regime, such as in recent femtosecond optical pump-probe studies on ionic crystals by Woerner *et al.* [26]. In the aforementioned study, the inhomogeneous screening was said to be caused by field-induced correlations between the valence and conduction band states. Third and finally, DFT has, in various realizations, become the primary theoretical tool for understanding dense plasma physics and nonequilibrium states of matter more generally, even if it is clear that further work is sorely needed to fully implement these methods at finite temperature [27–29]. Our work helps to define a new paradigm for testing different implementations of DFT by interrogating the central microscopic observable that is necessarily computed, namely $\rho(\vec{r})$. Prior work has not addressed how XRD is best used to differentiate between theories of electronic structure nor between the initial electronic heating and the subsequent lattice thermalization.

We emphasize here low-Z systems, a choice that is driven by the generic importance of low-Z materials for fusion-science applications and macromolecular studies and also by the observation that low-Z systems are also likely to have the largest effect on $S(\vec{Q})$ from valence electrons given their high fractional influence on the total charge density. The materials in the present study have been chosen to have wide contrast in ground-state electronic properties in order to investigate the diversity and generality of the reported phenomena. Specifically, we study extremely ionic LiF, metallic elemental Be, the strongly covalent insulator diamond, and the layered semimetal graphite. We predict testable changes in the XRD patterns at electronic temperatures from a few eV up to just below the onset of core ionization for each system. In these results we find extreme variation from system to system having a strong relationship with ground state electronic properties,

*seidler@uw.edu

emphasizing that the electronic structure of WDM has, in many ways, more heuristic commonalities with traditional condensed phase physics than it does with dense plasma physics.

II. THEORETICAL CONCEPT

A. Implications of the scattering factor formulation on the interpretation of XRD

Experimentally observed XRD intensities for momentum transfer $\vec{Q}$ are proportional to the square of the structure factor $S(\vec{Q})$,

$$S(\vec{Q}) \equiv \int_{\text{unit}} d^3 r \rho(\vec{r}) e^{-i\vec{Q}\cdot\vec{r}}, \tag{1}$$

where $\rho(\vec{r})$ is the electronic charge density, including both core and valence electrons, and the integral is performed over the unit cell. The effect of valence charge reorganization on $S(\vec{Q})$ can be made more apparent by recasting Eq. (1) as

$$S(\vec{Q}) = \int_{\text{unit}} dz \rho_{\vec{Q}}(z) e^{-iQz}, \tag{2}$$

where z is the parametric coordinate along the direction of $\vec{Q}$ and where the kernel of the transform $\rho_{\vec{Q}}(z)$ is the average of $\rho(\vec{r})$ over planes perpendicular to $\vec{Q}$. This formalism emphasizes the competing roles of charge on crystal planes and that within semilocalized interstitial bands. On the other hand, working from a simpler perspective, for perfectly crystalline systems it is common practice [19] to assume spherically symmetric charge distributions about each atom and to recast $S(\vec{Q})$ as

$$S(\vec{Q}) \cong \sum_j f_j(Q) e^{-i\ \vec{Q}\cdot\vec{r_j}}, \tag{3}$$

where $f_j(Q)$ is the atomic form factor (AFF) for species j. Some modern theories in plasma physics are not as simple as that given by Eq. (3) [16,30]. For example, in the spherically symmetric average-atom approximation, the unbound electrons are included as a screening field inside the Wigner-Seitz cell [31] [in Eq. (3) we neglect unbound electrons]. In what follows, we show that the nonuniform charge rearrangement into interstitial regions, an effect to which any fundamentally atomic mean-field or analytic treatment will be insensitive, is critical in determining the behavior of diffraction peak intensities at finite T.

The approximation presented in Eq. (3), which is known to have some measurable errors in strongly covalent systems [32–35], is not assumed *a priori* here for a reason centrally important to the electronic structure of WDM. Thermally activated electrons, although ubiquitously referred to as "free" electrons in the WDM and dense plasma literature [16], in fact strongly interact with the nuclear and semicore potentials and consequently are not in true momentum eigenstates, even if they may be in crystal-momentum eigenstates, i.e., Bloch waves (because of the comparative slowness of lattice relaxation). As such, unlike actual free electrons, the valence electrons in any dense system will contribute to the XRD at all T. We show here that these contributions are nontrivially material specific and, in several cases, quite large. Therefore, these effects can play a major role in the interpretation and design of XFEL-based XRD studies where x-ray heating is either intentional (such as to create warm dense matter states) or is a necessary consequence of the experiment (such as in macromolecular SFX).

B. Theoretical framework: DFT

The real space charge density was calculated from first principles using DFT, as implemented in the Vienna *ab initio* simulation package (VASP) [36]. The Perdew-Burke-Ernzerhof (PBE) functional was used for the generalized gradient approximation (GGA) to the exchange-correlation energy [37]. The projector augmented wave (PAW) method was used along with a plane-wave basis set for the electronic wave functions [38]. Excitation into higher Kohn-Sham orbitals was by virtue of the T dependence of the Fermi-Dirac occupancies [39]. The maximum simulated temperature for each material was chosen to be low enough such that less than 1% core ionization is anticipated. It is important to note that VASP uses a ground state exchange-correlation functional evaluated with a T-dependent density and, consequently, omits the intrinsic T dependence of the functional itself. While this simplification, which has often gone without comment in many VASP-based calculations in dense plasmas, can cause quantitative differences in total free energy, it is not expected to change the qualitative behavior of charge rearrangement at finite T for the present systems [27,40].

For the best approximation to the physical conditions for femtosecond-scale x-ray heating to electronic temperatures insufficient to cause core ionization, calculations were performed for frozen lattices in perfect crystals, where the ion locations and core electron occupancies and wave functions were not allowed to update. A sample VASP input file is provided as a supplement [41]. For each material, the charge density was sampled by splicing the unit cell into a fine grid. The grid density was chosen such that, via a numerical integral over the unit cell, we could reproduce the total charge to within an error of 10^{-3} electrons.

The structure factor was obtained by taking the discrete Fourier transform of $\rho(\vec{r})$, including both the frozen core contribution and that from the T-dependent valence charge distribution determined by the DFT code. The predicted scattering intensity, for a given $\vec{Q}$, is the squared modulus of $S(\vec{Q})$ [19]. Comparison to reference powder diffraction data showed excellent agreement after directionally averaging the calculated $S(\vec{Q})$.

For the purpose of comparing the VASP results to those acquired by assuming a spherically symmetric charge distribution, the atomic form factor, decomposed into subshells, was calculated through the use of the Cowan code [42]. The structure factor was then obtained via the standard sum over the basis atoms, i.e., Eq. (3). In order to study the effects of ionization on diffraction, the form factor of a given subshell was reduced by an amount corresponding to the percentage of valence electrons considered free. In an effort to compare the AFF and DFT results on an equal footing, ionization was obtained from a DFT calculation by dividing the occupancies of the valence orbitals at finite T by the same occupancies at 0 eV. Because the occupancies are obtained for a number of irreducible k points in the Brillouin zone, an average was taken.

III. RESULTS AND DISCUSSION

We present our central results in the eight panels of Fig. 1. From top to bottom, we show the dependence of the scattering intensity on temperature and ionization for selected Bragg reflections for LiF, graphite, diamond, and Be, all in their ambient, frozen lattice, and crystalline states. Table I lists the strength of the chosen reflections relative to each material's largest Bragg peak. The left column of Fig. 1 shows our finite-T DFT calculations, where the valence electrons were excited into low-lying unoccupied states having, as a rule, nontrivial spatial distribution and, consequently, nonzero contribution to $S(\vec{Q})$ in Eq. (1). Thus, the nominally ionized valence electrons play an important role in the XRD intensities at finite T, often having effects far larger than are discussed for ambient-T systems where modest aspherical corrections to $f(Q)$ are only occasionally required [34,35]. The results presented in the right column, on the other hand, were obtained using the simplest AFF model, i.e., Eq. (3), where the valence electrons were gradually removed from the atomiclike orbitals and consequently considered fully free, having no

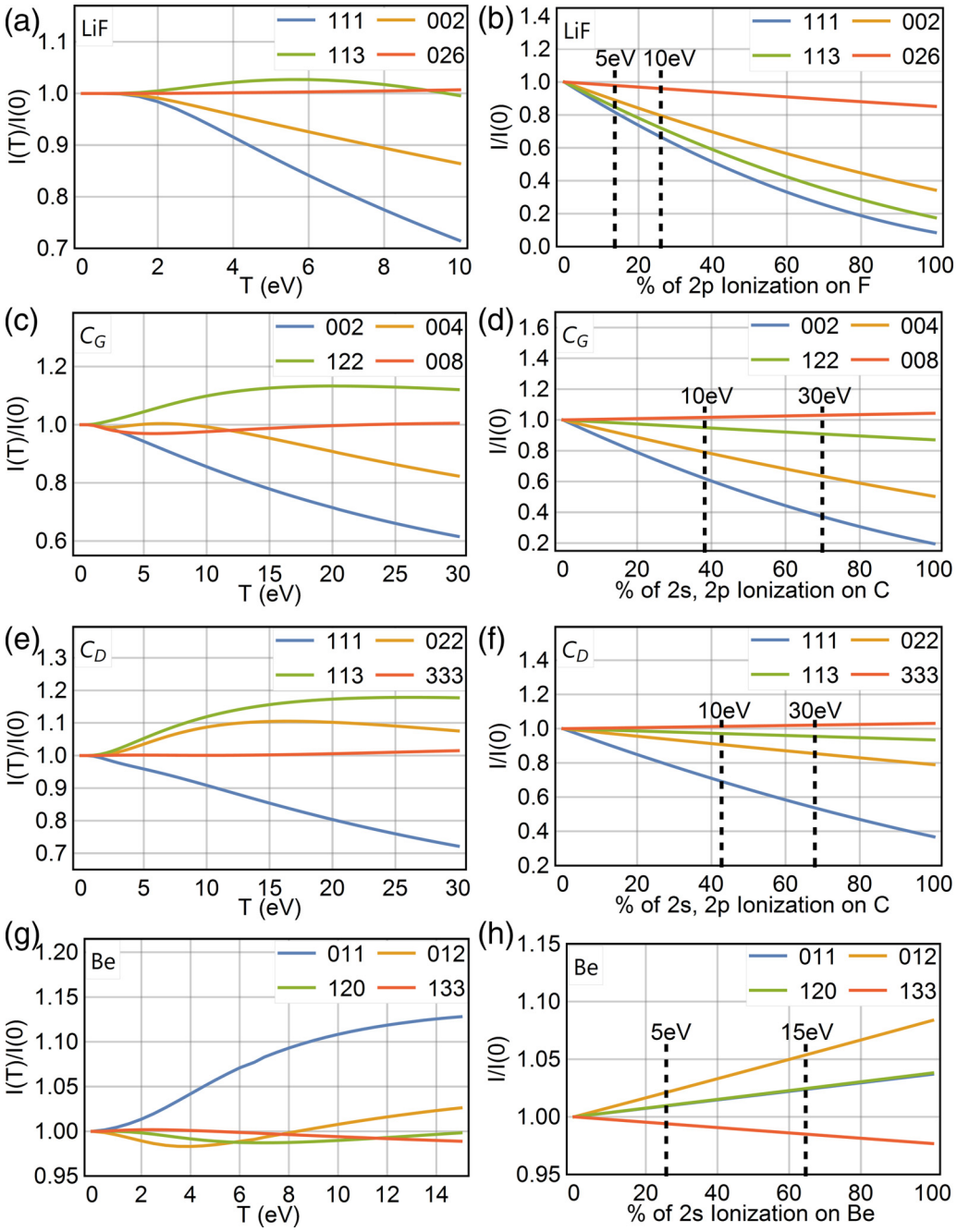

FIG. 1. A comparison of *ab initio* and atomic form factor XRD. Intensity of selected diffraction peaks as functions of temperature (left) and ionization (right), normalized to their values at 0 eV, for each of LiF, graphite (C_G), diamond (C_D), and Be. Peaks were chosen to capture a wide range in momentum transfer. The vertical lines mark points of equivalent ionization at a certain temperature in the DFT calculations. Note that the Be (011) is hidden by the (120) in (h).

TABLE I. XRD intensity data. Calculated Bragg intensities at $T = 0$ eV across all studied materials normalized to the sample's maximum reflection.

Material	Bragg peak	I/I_{max}
LiF	(111)	0.492
	(002)	0.893
	(113)	0.353
	(026)	0.322
Graphite	(002)	1.000
	(004)	0.368
	(122)	0.951
	(008)	0.124
Diamond	(111)	0.872
	(022)	0.941
	(113)	0.696
	(333)	0.618
Be	(011)	1.000
	(012)	0.282
	(120)	0.493
	(133)	0.529

contribution to $S(\vec{Q})$ after ionization. The vertical dashed lines in the AFF calculation panels are placed at the degree of ionization determined by the DFT calculations at the indicated temperatures, serving as convenient points of comparison between the results of the two calculations. The results presented in Fig. 1 yield several surprises that we now identify and explore.

To begin, in the heavily ionic LiF, the ground state valence electrons are located in the $2s$ and $2p$ bands of the F^- ion, while the higher energy bands are spatially arranged in the interstitial region between the F^- and Li^+ ions, see Fig. 2. This interstitial space is not uniformly filled, as would be assumed in a jellium or fully free electron model. These results at few-eV temperature are in good agreement with the prior work of Stegailov [43]. The two top panels in Fig. 1 give a direct comparison of the XRD predictions from DFT (left) and from the simple AFF model (right) for LiF. Comparing, for example, the $T = 10$ eV predictions for the DFT calculations and the corresponding results for the AFF calculation at equivalent ionization shows some general similarities in the behavior of several Bragg peaks but also a glaring inconsistency in the (113) reflection of LiF. In the AFF model, the loss of the $2p$ electrons on the F^- ion lead to a sharp decrease in $S(\vec{Q})$ for the (113) reciprocal lattice vector. However, in the DFT calculation, the rearrangement of valence charges onto planes of F^- ions (see Fig. 3), which make up the largest fraction of the total core density, leads to a slight increase in the (113) diffraction intensity for temperatures from 2 to 9 eV.

Another important case-in-point is illustrated by the behavior of graphite [Figs. 1(c), 1(d), 4, and 5] where the transfer of the valence charge density from the graphene sheets to the interstitial region is responsible for the strong finite-T quenching of the primary (002) peak but has less influence on the higher-harmonic c-axis reflections, such as the (004) or (008). This is because the very center of the interstitial region, where thermally excited charge first collects (see Fig. 4), is a

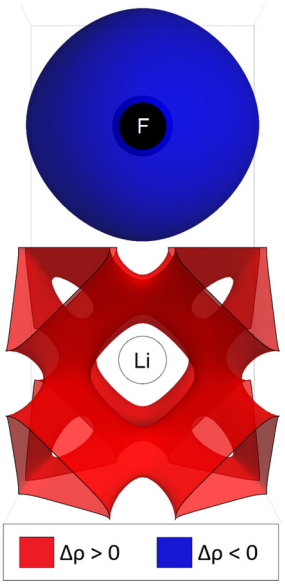

FIG. 2. Charge rearrangement of lithium fluoride. An illustration of the spatial rearrangement of valence charge density at a temperature of 3 eV within the LiF unit cell. Charge moves off the F^- ion ($\Delta\rho < 0$) and congregates in the interstitial region around the Li^+ ion ($\Delta\rho > 0$).

point of destructive interference for the (002) peak but not for higher harmonics, as per Eq. (2). Only at higher T, when the valence charge rearranges more uniformly in the interstitial space, will the higher harmonics begin to decrease. This is in stark contrast to the simple AFF calculation [Fig. 1(d)], wherein there are no strong interference effects associated with

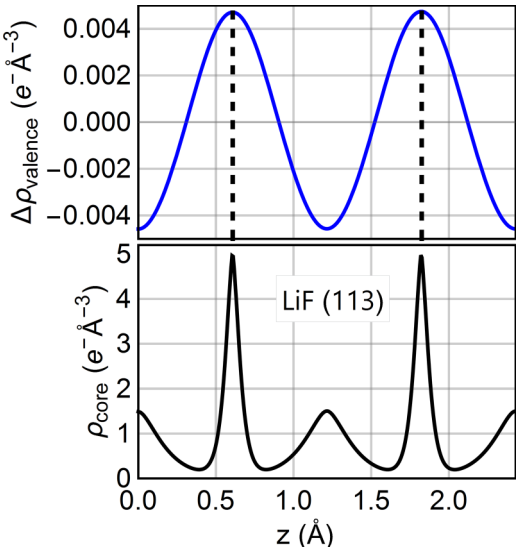

FIG. 3. Charge density along the (113) direction in LiF. The core charge density (bottom) and valence difference (top), $\Delta\rho = \rho(5\text{ eV}) - \rho(0\text{ eV})$, as a function of position along the (113) reciprocal lattice vector. The dotted vertical lines mark the positions of the F^- ions, demonstrating that as temperature increases, valence charge density moves off of Li^+ planes and onto the maximal regions of core density, thus resulting in an the increase in the (113) Bragg intensity seen in Fig. 1(a).

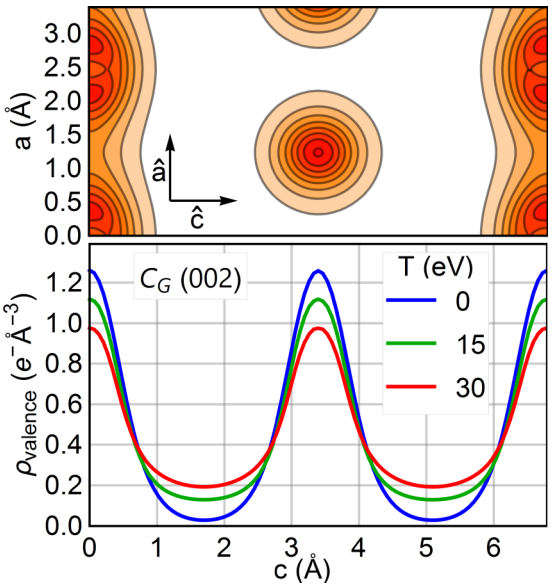

FIG. 4. Charge density along the [002] direction in graphite. (Top) A contour plot of the graphite unit cell viewed along the c axis. (Bottom) The valence charge density as a function of position along the c axis, for temperatures of 0, 15, and 30 eV.

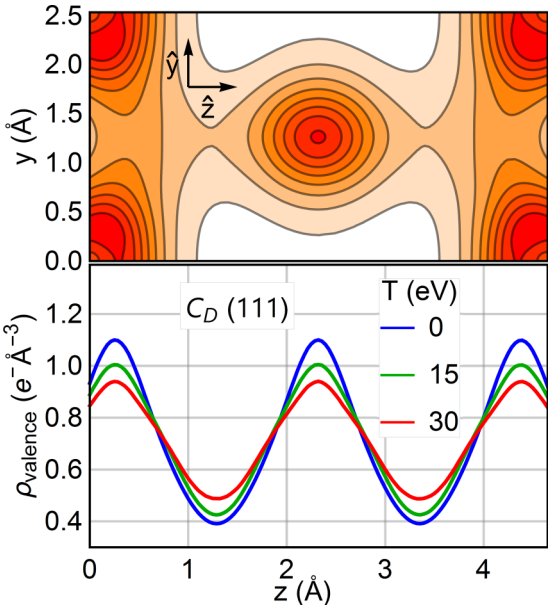

FIG. 6. Charge density along the (111) direction in diamond. (Top) A contour plot of the valence charge density in a diamond crystal viewed along the (111) reciprocal lattice vector at $T = 0$. (Bottom) The valence charge density as a function of position along the reciprocal lattice vector, for temperatures of 0, 15, and 30 eV. As temperature increases, valence charge density moves away from the ion cores, resulting in the decrease in (111) Bragg intensity seen in Fig. 1(e).

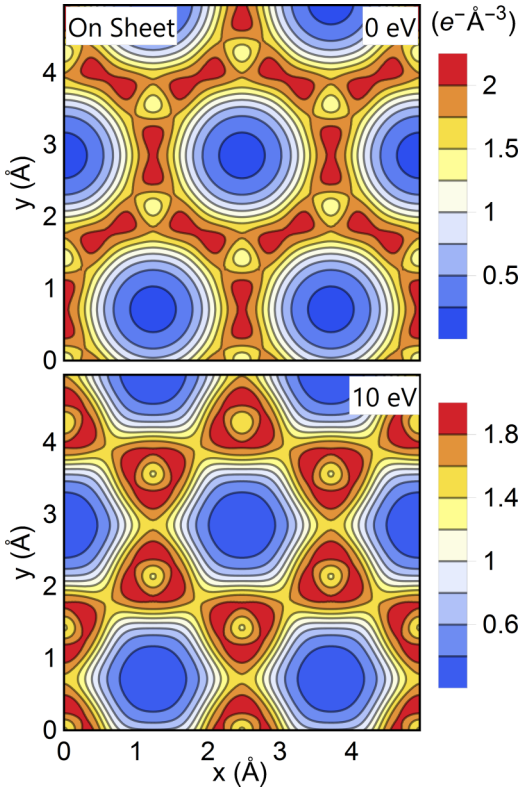

FIG. 5. Finite temperature charge reorganization in graphene sheets. Valence charge density on a graphene sheet within the extended unit cell of graphite at temperatures of 0 and 10 eV. Note the strong thermal depopulation of the ground state σ bonds. This effect decreases destructive interference in the (122) Bragg peak, resulting in the increase in Bragg intensity seen in Fig. 1(c).

ionized valence electrons and, thus, no delay in the quenching of the (004) Bragg intensity. Whether in their ground state or in a strongly thermally excited state, the relatively broad spatial distribution of valence electrons requires that they only play a role in low-Q XRD peaks, explaining why we see good agreement between the DFT and AFF results for the high-Q (008) harmonic.

This effect, in which charge reorganization upon electronic heating more preferentially influences the lower order harmonics, is also present in diamond [Figs. 1(e), 1(f), and 6] for which we see a large decrease in the (111) peak with little concomitant change in the (333) Bragg intensity. Harmonic disagreements such as these are likely to be a powerful effect with which to probe the competition and interplay between WDM electronic and ionic (lattice) structure upon XFEL heating: A decrease in, e.g., $I(002)/I(004)$ for graphite is necessarily an electronic effect, whereas a decrease in $I(004)/I(002)$ is instead a strong signature of lattice disorder. By contrast, the observation of a decrease in $I(002)$ for graphite, as in Hau-Riege *et al.* [7], without information about the evolution upon heating of any other Bragg peaks, is insufficient to separate the hypotheses of purely electronic heating with limited lattice response from that of a more fully thermalized energy cascade and consequent melting.

Returning to Fig. 1, we also observe several examples of increasing Bragg peak intensities. Perhaps most notably, for graphite, the (122) peak undergoes a 13% increase at 20 eV. This peak is sensitive to the changes in charge distribution parallel to the graphene sheets. In Fig. 5 we show the calculated valence charge distribution within a graphene sheet at $T = 0$

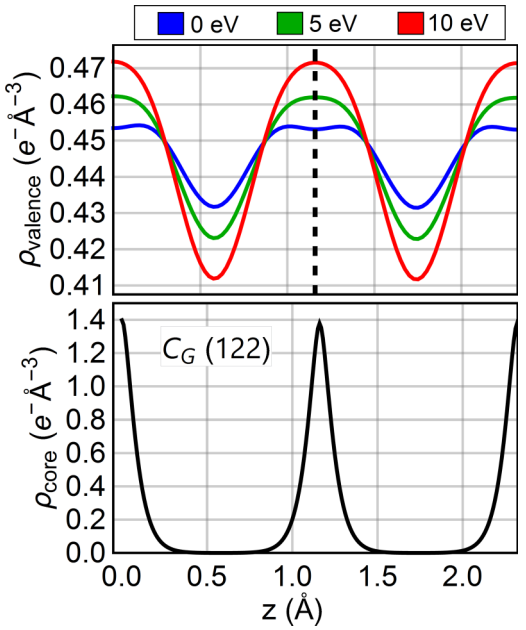

FIG. 7. Charge density along the (122) direction in graphite. The core (bottom) and valence (top) charge densities as a function of position along the (122) reciprocal lattice vector. The vertical line marks the position of the ion core, demonstrating that as temperature increases, valence charge density moves out of interstitial regions and onto the maximal regions of core density, resulting in the predicted increase in (122) Bragg intensity at elevated temperature shown in Fig. 1(c).

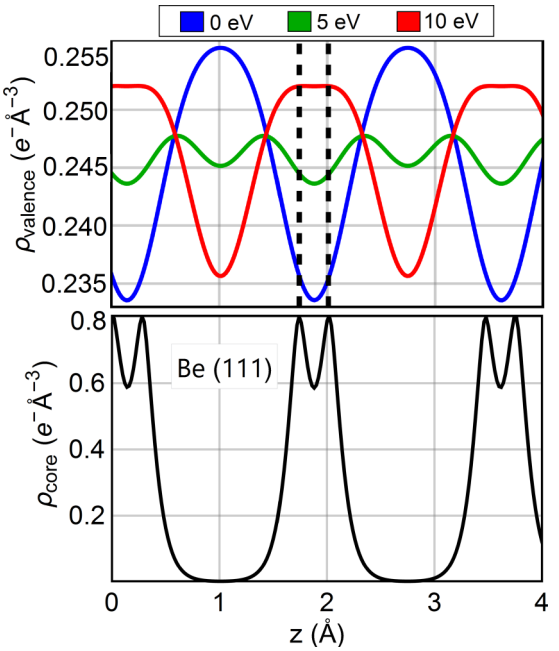

FIG. 8. Charge density along the (011) direction in beryllium. The core (bottom) and valence (top) charge density as a function of position along the (011) reciprocal lattice vector, for valence temperatures of 0, 5, and 10 eV. The vertical lines mark the positions of the Be ions for one period, demonstrating that as temperature increases, valence charge density moves out of interstitial regions and onto the ion cores, indicative of an increase in Bragg intensity.

and 10 eV. Here charge that was originally located in σ bonding orbitals has taken the spatial character of antibonding orbitals that are closer to the atoms. This new distribution increases constructive interference of the valence charge scattering with that from the ion cores resulting in an increase in the corresponding diffraction intensity, as shown in Fig 7. A similar behavior is responsible for what is essentially the only change in scattering intensities upon electronic heating in metallic Be. As T increases, valence charge moves closer to the Be atoms—a rearrangement that is favorable for constructive interference and leads to an increase in the (011) peak by 13% at 15 eV, as per Figs. 1(g), 1(h), and 8. While the AFF calculations do sometimes show small increases in Bragg peak intensity upon fractional ionization, as in the very similar (011) and (120) peaks, this is instead due to a decrease of destructive interference that had been due to the long tails of the assumed atomiclike valence wave functions.

Taken *en masse* our results require that the details of the finite-T valence charge rearrangement depends strongly on crystal structures and ground state electronic properties, having nontrivial consequences for XRD, as shown here, but also necessarily having nontrivial impact across all other observables. There is no generic jellium or other effective medium model that can capture the important spatial details of the manifestly system-specific reorganization of the real-space charge density upon heating. Ionization potential suppression, for example, should be similarly system specific because of the influence on screening of the (still) grossly inhomogeneous valence electron distribution at finite T. These effects should be particularly pronounced in crystal structures having strong anisotropy, e.g., graphite and other two-dimensional materials.

Before concluding, we also note that our results suggest important consequences for macromolecular crystallography studied at XFELs, where the long-term technical and scientific goal is to determine the structure of proteins and other biological macromolecules at atomic resolution [44,45]. The dominant paradigm in this field is commonly known as "diffract before destroy" [46–48], referring to the idea that useful diffraction data acquired at the beginning of the incident XFEL pulse, while the sample is intact and ion cores have not yet moved, is not adversely affected by the diffuse scattering signal acquired at the end of the pulse, when the sample is destroyed. However, it is unambiguous that electronic reorganization of the type discussed here must precede ion motion: it is the reorganization of the real-space charge density combined with the decreasing electronic degeneracy that results in the large, unbalanced forces that drive any ultrafast motion of the lattice. The diffraction signal prior to "destruction" necessarily includes a time average over a strong electronic reorganization of valence electrons and also a nontrivial reorganization of core or semicore electrons. Present-day XFEL results are not impacted by the foregoing observation due to the typical spatial resolution of ~10 Å [45,46,48,49]. However, when the goal of atomic resolution is attained and biological and photochemical processes are probed at the most basic level, a more complete theoretical treatment of the electronic structure will be necessary.

IV. CONCLUSION

In this paper we have shown that thermally excited and often significantly delocalized valence electrons still have a direct, measurable effect on the experimental observable of x-ray diffraction. These effects have specific consequences that can be tested in detail with wide-angle scattering studies that, for example, allow the comparison of the temperature dependence of intensities of low-order Bragg reflections with their higher harmonics. This will pose new challenges for accelerator operations, as an optimal XRD study on x-ray heated warm dense matter might then be to use a lower energy pump pulse (to maximize energy density deposition) and higher energy, such as third harmonic, probe pulse (to maximize the momentum transfer range being interrogated). Finally, the continued importance in XRD of the detailed valence-level electronic structure, even at many-eV temperatures, suggests an important endpoint to the applicability of the "diffract before destroy" paradigm in macromolecular SFX at XFELs.

ACKNOWLEDGMENTS

We thank Sam Trickey, John Rehr, Fernando Vila, Joshua Kas, and Micah Prange for useful discussions. This work was supported by the US Department of Energy, Office of Science, Fusion Energy Sciences and the National Nuclear Security Administration under Grant No. DE-SC0008580. This research used resources of the National Energy Research Scientific Computing Center, a DOE Office of Science User Facility supported by the Office of Science of the U.S. Department of Energy under Contract No. DE-AC02-05CH11231.

[1] C. Svetina *et al.*, J. Synchrotron Radiat. **22**, 538 (2015).
[2] W. E. White, A. Robert, and M. Dunne, J. Synchrotron Radiat. **22**, 472 (2015).
[3] M. Yabashi, H. Tanaka, and T. Ishikawa, J. Synchrotron Radiat. **22**, 477 (2015).
[4] E. Allaria *et al.*, J. Synchrotron Radiat. **22**, 485 (2015).
[5] H. Wabnitz *et al.*, Nature (London) **420**, 482 (2002).
[6] L. Young *et al.*, Nature (London) **466**, 56 (2010).
[7] S. P. Hau-Riege *et al.*, Phys. Rev. Lett. **108**, 217402 (2012).
[8] B. Nagler *et al.*, Nat. Phys. **5**, 693 (2009).
[9] B. F. Murphy *et al.*, Nat. Commun. **5**, 4281 (2014).
[10] S. M. Vinko *et al.*, Nature (London) **482**, 59 (2012).
[11] B. I. Cho *et al.*, Phys. Rev. Lett. **109**, 245003 (2012).
[12] A. A. Lutman, R. Coffee, Y. Ding, Z. Huang, J. Krzywinski, T. Maxwell, M. Messerschmidt, and H. D. Nuhn, Phys. Rev. Lett. **110**, 134801 (2013).
[13] A. Marinelli *et al.*, Nat. Commun. **6**, 6369 (2015).
[14] E. Allaria *et al.*, Nat. Commun. **4**, 2476 (2013).
[15] M. Cooper, *X-ray Compton Scattering*, Oxford series on synchrotron radiation, Vol. 5 (Oxford University Press, Oxford, 2004).
[16] S. H. Glenzer and R. Redmer, Rev. Mod. Phys. **81**, 1625 (2009).
[17] F. d. Groot and A. Kotani, *Core Level Spectroscopy of Solids*, Advances in Condensed Matter Science (CRC Press, Boca Raton, FL, 2008), Vol. 6.
[18] J. Als-Nielsen and D. McMorrow, *Elements of Modern X-ray Physics*, 2nd ed. (Wiley-Blackwell, Oxford, 2011).
[19] C. Kittel, *Introduction to Solid State Physics*, 8th ed. (Wiley, Hoboken, NJ, 2005).
[20] R. P. Drake, *High-Energy-Density Physics: Fundamentals, Iinertial Fusion, and Experimental Astrophysics* (Springer, Berlin, New York, 2006), shock wave and high pressure phenomena.
[21] G. Ecker and W. Kroll, Phys. Fluids **6**, 62 (1963).
[22] L. B. Fletcher *et al.*, Phys. Rev. Lett. **112**, 145004 (2014).
[23] J. C. Stewart and K. D. Pyatt, Astrophys. J. **144**, 1203 (1966).
[24] S. M. Vinko, O. Ciricosta, and J. S. Wark, Nat. Commun. **5**, 3533 (2014).
[25] O. Ciricosta *et al.*, Phys. Rev. Lett. **109**, 065002 (2012).
[26] M. Woerner, M. Holtz, V. Juve, T. Elsaesser, and A. Borgschulte, Faraday Discuss. **171**, 373 (2014).
[27] V. V. Karasiev, T. Sjostrom, J. Dufty, and S. B. Trickey, Phys. Rev. Lett. **112**, 076403 (2014).
[28] M. Greiner, P. Carrier, and A. Gorling, Phys. Rev. B **81**, 155119 (2010).
[29] R. A. Lippert, N. A. Modine, and A. F. Wright, J. Phys. Condens. Matter **18**, 4295 (2006).
[30] G. Gregori, A. Ravasio, A. Holl, S. H. Glenzer, and J. Rose, High Energy Density Phys. **3**, 99 (2007).
[31] W. R. Johnson, J. Nilsen, and K. T. Cheng, Phys. Rev. E **86**, 036410 (2012).
[32] C. Jelsch, M. M. Teeter, V. Lamzin, V. Pichon-Pesme, R. H. Blessing, and C. Lecomte, Proc. Natl. Acad. Sci. USA **97**, 3171 (2000).
[33] N. K. Hansen and P. Coppens, Acta Crystallogr. Sect. A **34**, 909 (1978).
[34] A. Volkov, M. Messerschmidt, and P. Coppens, Acta Crystallogr. Sect. D **63**, 160 (2007).
[35] D. Jayatilaka and B. Dittrich, Acta Crystallogr. Sect. A **64**, 383 (2008).
[36] G. Kresse and J. Furthmuller, Phys. Rev. B **54**, 11169 (1996).
[37] J. P. Perdew, K. Burke, and M. Ernzerhof, Phys. Rev. Lett. **77**, 3865 (1996).
[38] G. Kresse and D. Joubert, Phys. Rev. B **59**, 1758 (1999).
[39] N. D. Mermin, Phys. Rev. **137**, A1441 (1965).
[40] V. V. Karasiev, T. Sjostrom, and S. B. Trickey, Phys. Rev. E **86**, 056704 (2012).
[41] See Supplemental Material at http://link.aps.org/supplemental/10.1103/PhysRevB.93.115135 for the Vienna ab-initio simulation package, demonstrating how we set up a frozen lattice calculation with finite electronic temperature.
[42] R. D. Cowan, *The Theory of Atomic Structure and Spectra*, Los Alamos series in basic and applied sciences, Vol. 3 (University of California Press, Berkeley, 1981).
[43] V. V. Stegailov, Contrib. Plasma Phys. **50**, 31 (2010).
[44] A. Barty, J. Kupper, and H. N. Chapman, Annu. Rev. Phys. Chem. **64**, 415 (2013).
[45] J. C. H. Spence, U. Weierstall, and H. N. Chapman, Rep. Prog. Phys. **75**, 102601 (2012).
[46] H. N. Chapman, C. Caleman, and N. Timneanu, Philos. Trans. R. Soc. London Ser. B **369**, 20130313 (2014).
[47] A. Doerr, Nat. Methods **8**, 283 (2011).
[48] C. Caleman, N. Timneanu, A. V. Martin, H. O. Jonsson, A. Aquila, A. Barty, H. A. Scott, T. A. White, and H. N. Chapman, Opt. Express **23**, 1213 (2015).
[49] B. D. Patterson, Crystallogr. Rev. **20**, 242 (2014).